

# 1 An isolated, bright cusp aurora at Saturn

2  
3 J. Kinrade<sup>1</sup>, S. V. Badman<sup>1</sup>, E. J. Bunce<sup>2</sup>, C. Tao<sup>3</sup>, G. Provan<sup>2</sup>, S. W. H. Cowley<sup>2</sup>, A. Grocott<sup>1</sup>, R. L.  
4 Gray<sup>1</sup>, D. Grodent<sup>4</sup>, T. Kimura<sup>5</sup>, J. D. Nichols<sup>2</sup>, C. S. Arridge<sup>1</sup>, A. Radioti<sup>4</sup>, J. T. Clarke<sup>6</sup>, F. J. Crary<sup>7</sup>,  
5 W. R. Pryor<sup>8</sup>, H. Melin<sup>2</sup>, K. H. Baines<sup>9</sup>, M. K. Dougherty<sup>10</sup>

6  
7 <sup>1</sup>Department of Physics, Lancaster University, Lancaster, LA1 4YB, UK

8 <sup>2</sup>Department of Physics & Astronomy, University of Leicester, Leicester, LE1 7RH UK

9 <sup>3</sup>Space Environment Laboratory, National Institute of Information and Communications Technology  
10 (NICT), Koganei, Tokyo, Japan

11 <sup>4</sup>LPAP, Institut d'Astrophysique et de Géophysique, Université de Liège, Liège, Belgium

12 <sup>5</sup>RIKEN Nishina Center for Accelerator-Based Science, Saitama, Japan

13 <sup>6</sup>Department of Astronomy and Center for Space Physics, Boston University, USA

14 <sup>7</sup>LASP, University of Colorado Boulder, Boulder, Colorado, USA

15 <sup>8</sup>Dept. of Science, Central Arizona College, Coolidge, Arizona, USA

16 <sup>9</sup>Jet Propulsion Laboratory, California Institute of Technology, Pasadena, California, USA

17 <sup>10</sup>Space and Atmospheric Physics Group, Blackett Laboratory, Imperial College London, London, UK

18  
19 Corresponding author: Joe Kinrade, Department of Physics, Lancaster University, Bailrigg, Lancaster,  
20 LA1 4YB, j.kinrade@lancaster.ac.uk.

## 21 Abstract

22  
23  
24 Saturn's dayside aurora display a number of morphological features poleward of the main emission  
25 region. We present an unusual morphology captured by the Hubble Space Telescope on 14 June 2014  
26 (day 165), where, for two hours, Saturn's FUV aurora faded almost entirely, with the exception of a  
27 distinct emission spot at high latitude. The spot remained fixed in local time between 10-15 LT, and  
28 moved polewards to a minimum colatitude of  $\sim 4^\circ$ . It was bright and persistent, displaying intensities of  
29 up to 49 kR over a lifetime of two hours. Interestingly the spot constituted the entirety of the northern  
30 auroral emission, with no emissions present at any other local time – including Saturn's characteristic  
31 dawn arc, the complete absence of which is rarely observed. Solar wind parameters from propagation  
32 models, together with a Cassini magnetopause crossing and solar wind encounter, indicate that Saturn's  
33 magnetosphere was likely to have been embedded in a rarefaction region, resulting in an expanded  
34 magnetosphere configuration during the interval. We infer that the spot was sustained by reconnection  
35 either poleward of the cusp, or at low latitudes under a strong component of interplanetary magnetic  
36 field transverse to the solar wind flow. The subsequent poleward motion could then arise from either  
37 reconfiguration of successive open field lines across the polar cap, or convection of newly opened field  
38 lines. We also consider the possible modulation of the feature by planetary period rotating current  
39 systems.

## 40 Key Points

- 41  
42  
43
  - 44 ■ Saturn's dawn arc auroral emission was observed to fade strongly for several hours.
  - 45 ■ This may have been attributable to reduced plasma flow shear during a prolonged solar wind rarefaction.
  - 46 ■ An isolated auroral spot emission is evidence of dayside reconnection at an expanded
  - 47 magnetosphere.

## 1 Introduction

Detections of dayside reconnection signatures at Saturn provide evidence of the solar wind influence on magnetospheric and ionospheric dynamics. Auroral imagery offers a valuable way of remotely detecting the occurrence of reconnection.

Earth's dayside auroral morphology has a well-studied response to the solar wind interaction [e.g. Milan et al., 2010] and Dungey [1961] circulation of the magnetosphere. Low latitude reconnection between a southward interplanetary magnetic field (IMF) and planetary field at the dayside magnetopause, resulting in open flux production, generates a cusp spot just equatorward of the open-closed field line boundary (OCB) and poleward moving forms [e.g. Milan et al., 2000a]. Reconnection at high latitudes between a northward IMF and the open lobe field lines generates an auroral spot just poleward of the OCB and equatorward moving arcs [e.g. Øieroset et al., 1997; Milan et al., 2000b; Frey et al., 2002]. Signatures of high latitude dayside reconnection and cusp precipitation in the terrestrial aurora are correlated with solar wind density (affecting emission intensity) and the transverse IMF component (controlling local time position) [e.g. Milan et al., 2000b; Frey et al., 2002; Fuselier et al., 2002; Fear et al., 2015].

Saturn's auroras, however, are the product of a highly rotational magnetosphere, displaying clear responses to both the solar wind [e.g. Clarke et al., 2005; 2009; Crary et al., 2005] and internal plasma sources [e.g. Mitchell et al., 2009]. The main auroral emission is driven by flow shears in the outer magnetosphere, initially thought to map to an upward current region near the OCB [e.g. Cowley et al., 2004; Bunce et al., 2008]. Subsequent detailed studies have shown that the maximum upward field-aligned currents (FAC) map to a region 1-2° equatorward of the OCB, suggesting an additional dependence on the ionospheric conductivity [e.g. Talboys et al., 2009; Jinks et al., 2014; Hunt et al., 2015]. A persistent dawn arc shows little dependence on IMF direction [Meredith et al., 2014] in comparison to the strong auroral modulation by the IMF observed at Earth [e.g. Milan et al., 2010]. Mapping to the outer ring current region [Belenkaya et al., 2014], the dawn arc has been observed to expand and brighten in response to tail reconnection events [Mitchell et al., 2009; Nichols et al., 2014; Radioti et al., 2014; 2016; Badman et al., 2016] and hot plasma injections in the absence of solar wind triggering [e.g. Gérard et al., 2006]. Absence of the dawn arc has only occasionally been observed [e.g. Nichols et al., 2016].

Spiral forms encircling the entire auroral region have been observed in response to solar wind compression dynamics [e.g. Clarke et al., 2005; Cowley et al., 2005]. Grodent et al. [2005] reported sub-corotating auroral features at Saturn during quiet solar wind conditions, when an emission spot was observed to decelerate in angular velocity from 70% to 20% of corotation as it moved past noon, reducing in brightness and moving rapidly poleward by ~10° at the same time. This feature rotated from dawn before this point, and similar features have been interpreted as signatures of nightside plasma injection [Cowley et al., 2005; Lamy et al., 2013; Nichols et al., 2014] or propagating ULF waves [Meredith et al., 2013].

The efficiency of magnetopause reconnection at Saturn has been questioned because of the different plasma environments and velocity flow shear on either side of the magnetopause compared to the Earth [e.g. Masters et al., 2012; Desroche et al., 2013]. However, various auroral and in situ signatures of reconnection have been identified. Low-latitude reconnection signatures in Saturn's auroras appear as intensifications within the main emission in the noon-dusk region that subsequently bifurcate polewards [Radioti et al., 2011; Badman et al., 2013; Jasinski et al., 2014]. These bifurcations are sometimes observed to pulse in intensity with a ~1 h period and have poleward speeds of ~2° per hour [Radioti et al., 2013; Mitchell et al., 2016; Nichols et al., 2016]. There is some evidence that these auroral bifurcations are more likely to occur when the magnetosphere is compressed [Badman et al., 2013]. Simultaneous HST observations and Cassini measurements of the upstream solar wind revealed that Saturn's dayside auroras have a dependency on IMF polarity [Meredith et al., 2014], with patchy post-noon emissions (possibly bifurcations not resolved by HST) visible during periods of positive  $B_z$  but absent during negative  $B_z$ ; Saturn's magnetic dipole has opposite direction to Earth's.

In addition to auroral observations, in situ Cassini measurements of heated magnetosheath plasma, a component of the magnetic field normal to the magnetopause [McAndrews et al., 2008], and escaping magnetospheric electrons [Badman et al., 2013] have indicated reconnection activity at the low-latitude magnetopause. Magnetosheath plasma has been identified in Saturn's magnetospheric cusps, including

108 stepped ion dispersion signatures indicating bursty reconnection [Jasinski et al., 2014; Arridge et al.,  
109 2016]. Jasinski et al. [2016] have identified a dayside flux transfer event, confirming that Saturn’s  
110 magnetopause is conducive to multiple reconnection sites and open flux generation.

111  
112 High-latitude (i.e. poleward of the cusp) reconnection signatures, reminiscent of those seen under  
113 northward IMF conditions at Earth, have also been observed [Gérard et al., 2005; Badman et al., 2013;  
114 Mitchell et al., 2016; Palmaerts et al., 2016]. Gérard et al. [2005] investigated a cusp spot signature  
115 fixed at noon local time for at least 30 minutes during an interval of intermediate IMF strength  
116 following a minor compression of the solar wind. These observations were generally consistent with  
117 the model of Bunce et al. [2005], which estimates reconnection-driven flows and resulting polar cusp  
118 UV auroral emissions for different IMF conditions. Meredith et al. [2014] observed a high-latitude,  
119 pre-noon emission signature during a period of upstream southward IMF, extending from the main  
120 dawn arc emission to the spin pole itself. This case was attributed to lobe reconnection, consistent with  
121 the high latitude of the emission and the expected location of the magnetopause reconnection site  
122 during southward IMF at Saturn.

123  
124 In addition to these solar wind-driven signatures, Saturn’s auroral emissions also display a rotational  
125 modulation in intensity and location. Based on observations of near-planetary period oscillations (PPO)  
126 in the magnetic field, this modulation is attributed to a system of FACs rotating independently, and  
127 with slightly different periods, in the northern and southern hemispheres [e.g. Provan et al., 2009;  
128 2016; Andrews et al., 2010; Hunt et al., 2014]. Auroral emission intensity increases where the rotating  
129 FAC system is directed upward (implying downward precipitating electrons) [e.g. Badman et al.,  
130 2012]. The intensity of the dawn arc is modulated by PPO phase in the southern hemisphere, but this  
131 variation is not as clear in the northern hemisphere [Nichols et al., 2010; 2016]. The additional  
132 magnetic field component of the PPO perturbations effectively tilts Saturn’s background field, and the  
133 entire oval oscillates by up to several degrees of latitude with the PPO phase [Nichols et al., 2008;  
134 2010; 2016].

135  
136 The paucity of studies combining auroral imagery, Cassini magnetopause encounters and reliable  
137 upstream solar wind monitoring at Saturn means that further observations are required to understand  
138 the dayside reconnection processes and their role in driving auroral currents and plasma flows. In this  
139 case study we report on Hubble Space Telescope (HST) observations of Saturn’s northern FUV auroras  
140 on 14 June 2014, together with in situ Cassini measurements of the upstream solar wind conditions and  
141 magnetopause location. Observations from three consecutive HST orbits on this day revealed a period  
142 of unusually quiet emission morphology, with the exception of an isolated, bright poleward signature  
143 that persisted for several hours on the dayside. Here we investigate the potential drivers of the auroral  
144 emission in the context of dayside reconnection under expanded magnetospheric conditions. We also  
145 discuss the possible modulation of the auroral signature by the rotating planetary-period current  
146 system.

147

## 148 2 Data

149

### 150 2.1 HST STIS pipeline

151

152 The HST Space Telescope Imaging Spectrograph (STIS) captured the images used in this study, during  
153 three HST orbits on 14 June 2014 (day 165). The instrument’s SrF2 filter excludes hydrogen Lyman  
154 alpha emission at 121.6 nm, but passes the H<sub>2</sub> Lyman and Werner bands in the range 125-190 nm.  
155 Systematic image processing followed the pipeline steps developed by Boston University [Clarke et al.,  
156 2009; Nichols et al., 2009], including flat-fielding, dark count subtraction, and correction for geometric  
157 distortion. Emissions from the planetary disk and geocorona were also removed using the same method  
158 as Clarke et al. [2009] i.e. determining best fit Minnaert coefficients for the center-to-limb variation  
159 and using a latitudinal intensity profile extrapolated over the auroral region. Close to the auroral region  
160 the uncertainty in the empirically derived background is ~2-3 kR. The images were scaled to a standard  
161 distance between HST and Saturn of ~8.2 AU, and projected onto a 0.25° × 0.25° planetocentric  
162 latitude and longitude grid at an emission altitude of 1100 km above the 1 bar pressure level [Gérard et  
163 al., 2009]. The STIS MAMA detector consists of 1024 × 1024 pixels, with a single pixel dimension of  
164 0.025 arc sec; this translates to a range of distances subtended by a single pixel projected on the planet  
165 surface, but at nadir this is ~476 km with an Earth-Saturn distance of 8.2 AU and taking account of the  
166 ~0.08 arc sec point spread function. Spatial uncertainties in the images arise, however, from  
167 determination of the planet center and distortion of projected pixels towards the limb; Grodent et al.

168 [2003] showed that this spatial uncertainty is  $\sim 1^\circ$  for typical observation geometries ( $\sim 1000$  km on the  
169 planet surface).

170

171 Exposure times ranged between  $\sim 700$ - $840$  s. Photon count rates were converted to intensity values of  
172 unabsorbed  $H_2$  emission across the wavelength range 70-180 nm using the conversion factor of  $1 \text{ kR} =$   
173  $3994$  counts per second given by Gustin et al. [2012], assuming a color ratio of 1.1 across Saturn's  
174 auroral region.

175

## 176 2.2 Upstream solar wind conditions

177

178 The Cassini spacecraft entered the solar wind on day 160 for several hours, with the magnetometer  
179 (MAG) [Dougherty et al., 2004] instrument providing measurement of the IMF conditions upstream of  
180 Saturn (five days prior to the auroral observations). Plasma measurements from the CAPS instrument  
181 were not available during the study period. Magnetic field measurements and spacecraft position are  
182 given in Kronocentric Solar Magnetospheric (KSM) coordinates, which have Saturn at the origin; the X  
183 axis is directed towards the Sun, Z is defined such that Saturn's rotation and magnetic axis lies in the  
184 XZ plane, and Y lies in Saturn's rotation and magnetic equatorial plane [Dougherty et al., 2005]. The  
185 solar wind encounter was identified by the sharp decrease in IMF magnitude as Cassini left the  
186 magnetosheath. We used this period to verify the validity of the solar wind projection models described  
187 below. Several days later, between days 163 and 164, Cassini crossed the magnetopause boundary  
188 inbound, followed by an excursion back into the magnetosheath before re-entering the magnetosphere.  
189 We used the position of Cassini at these crossing times to estimate the dynamic pressure and sub-solar  
190 standoff distance of the magnetopause, using the Kanani et al. [2010] magnetopause model.

191

192 In addition to the in situ Cassini measurements, we used projections from two 1D-MHD propagation  
193 models to gauge incident solar wind conditions during the HST observation period. Both the Michigan  
194 Solar Wind Model (mSWiM) [Zeiger & Hansen, 2008] and Tao et al. [2005] models project multi-  
195 spacecraft measurements at 1 AU provided by the OMNIweb service, using the source satellite that is  
196 closest to opposition with the desired target. Conditions for projection are optimal at opposition, when  
197 the actual boundary conditions at 1 AU are propagated, including transient signatures like shock fronts.  
198 Day 165 of 2014 was within four days of apparent Earth-Saturn opposition (actual opposition plus  
199 approximate solar wind travel time to Saturn) on day 161. Solar wind velocity is the most accurately  
200 modeled parameter (based on correlation with 12 years of in situ measurements from the Voyager,  
201 Pioneer and Ulysses missions [Zeigler & Hansen, 2008]), followed by IMF magnitude, number density  
202 and transverse field components. Accurate estimation of the IMF  $B_z$  component is not possible with  
203 single-dimension MHD solar wind models. Dynamic pressure,  $P_{\text{DYN}}$ , was obtained by converting the  
204 number density to a mass density,  $\rho$ , and then multiplying by the summed-squared velocity components  
205 ( $P_{\text{DYN}} = \rho v^2$ ). The input data availability from OMNIweb was  $\sim 97\%$  for 2014, and the solar wind speed  
206 recurrence index (a measure of solar wind speed consistency between successive solar rotations) was  
207 low (0.17) during essentially the maximum period of the solar cycle – both of these factors are  
208 important for reliable solar wind prediction at 10 AU, the outer boundary of the models. The impact of  
209 low solar wind speed recurrence on the model's prediction efficiency is minimal during apparent  
210 opposition, however we added a conservative  $\pm 40$  h uncertainty window to the solar wind parameters  
211 (see Figure 11 of Zeiger & Hansen [2008]).

212

## 213 3 Observations

214

### 215 3.1 Solar wind models

216

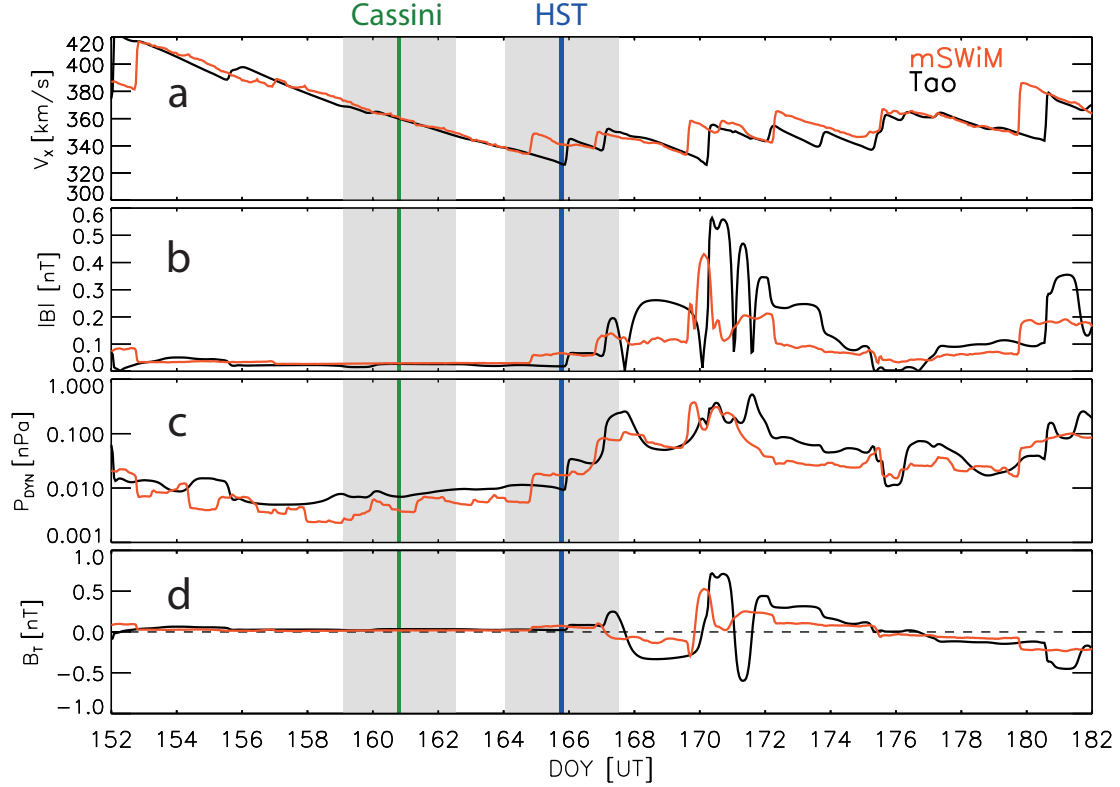


Figure 1. Solar wind parameters throughout June 2014, as projected using two different 1-D MHD models. mSWiM parameters [Zeiger & Hansen, 2008] are plotted in red, and those from the Tao et al. [2005] model in black. The top plot shows the component of solar wind velocity directed radially outward from the Sun,  $V_x$  (1a), followed by IMF magnitude (1b), dynamic pressure (1c, logarithmic scale) and transverse IMF component in the Radial-Tangential-Normal (RTN) frame (positive  $B_T \approx$  negative  $B_Y$  in the KSM frame) (1d). For reference the blue vertical line marks the extent of the HST imaging window on day 165, and the green line marks the  $\sim 2$  hr time window of solar wind measurement made by Cassini on day 160 (see Section 3.2). The two grey shaded regions represent conservative  $\pm 40$  hr uncertainty windows for the model projections i.e. model parameters within the blue or green-shaded times could take any value within the respective grey-shaded uncertainty region.

Both solar wind projection models indicate a gradual decrease in velocity over the two weeks prior to the observation window (blue vertical line in Figure 1), from  $\sim 420 \text{ km s}^{-1}$  to below  $350 \text{ km s}^{-1}$ . The magnitude of the IMF,  $|B|$ , was also low throughout this period ( $< 0.1 \text{ nT}$ ), with the exception of a small increase to  $\sim 0.2 \text{ nT}$  on day 167 (the end of the uncertainty window shown by the grey-shaded region in Figure 1). The trend in dynamic pressure was similar, being between  $0.001$ - $0.005 \text{ nPa}$  until an apparent region of solar wind disturbance beginning on day 167 that persisted for a week afterwards.

Finally, the transverse  $B_T$  component was positive ( $\sim 0.1 \text{ nT}$ ) for an extended period including the observation window. Generally the estimated parameters are similar in both projection models and consistent with a period of rarefaction at Saturn preceding the HST observation window on day 165; we discuss this further in Section 4.1. In the next section we compare these projected magnetic parameters with IMF measurements from Cassini during a brief solar wind encounter on day 160.

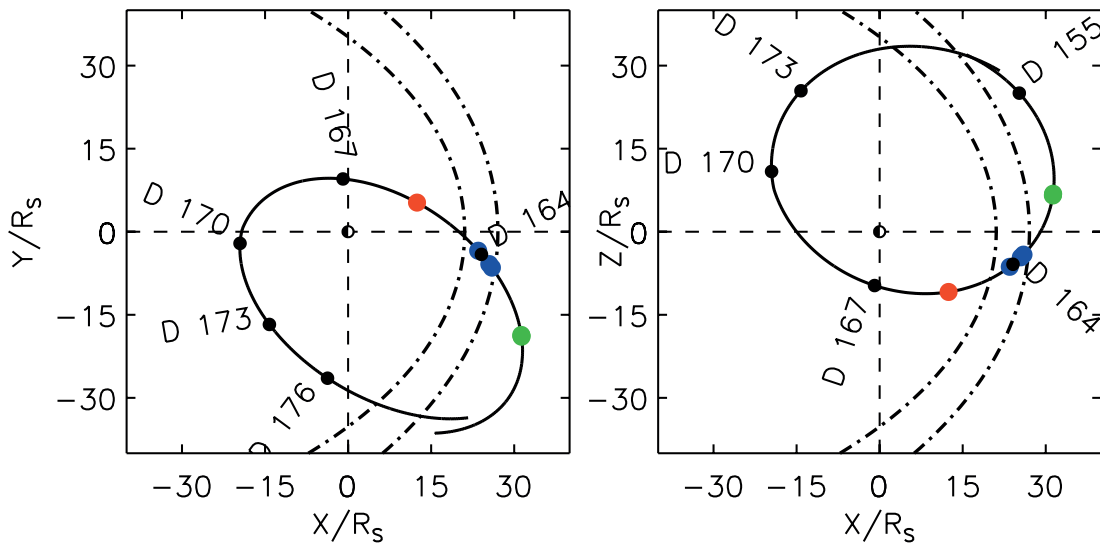
A wider picture of the solar wind activity from projections over April, May and June 2014 (not shown here), indicated that the period of disturbance between days 167-175 (see Figure 1) may have originated from a mix of Corotating Interaction Region (CIR) and Interplanetary Coronal Mass Ejection-like (ICME) structuring recorded at 1 AU around days 120-121 of 2014. Prior to this disturbance the solar wind velocity appears to have been remarkably low for  $\sim 1$  month, falling to below  $300 \text{ km s}^{-1}$  at times and approaching the slowest solar wind speeds encountered at 1 AU [Sanchez-Diaz et al., 2016]. It's possible that this case study captures an auroral morphology at Saturn during a prolonged period of extremely quiet ambient solar wind.

252 3.2 In situ Cassini measurements

253

254 We examine in situ Cassini magnetometer measurements to determine both upstream conditions in the  
 255 solar wind and how compressed the magnetosphere was. Prior to the HST observations, from day 160  
 256 onwards, Cassini's orbit was inbound, crossing the equatorial plane close to local noon on day 164.

257 Cassini's trajectory (KSM coordinates) during revolution 205 is shown in Figure 2, with annotation  
 258 showing the spacecraft location at the time of HST observations on day 165 (red dot). Figure 2a shows  
 259 the orbital trace (solid black line) as viewed from above the northern hemisphere in the KSM X-Y  
 260 plane, and Figure 2b as viewed from the dawn flank in the KSM X-Z plane. The Sun is to the right of  
 261 the figure in each case. Black dots show Cassini's position on the days annotated. Further annotation is  
 262 based on Cassini MAG measurements discussed below (see Figure 3), namely a solar wind encounter  
 263 on day 160 (green dot) and several magnetopause crossings on days 163-164 (blue dots). For reference  
 264 and based on these crossings, two magnetopause positions are shown in Figure 2 at standoff distances  
 265 of  $24 R_S$  and  $27 R_S$  (dot-dash lines), obtained using the Kanani et al. [2010] magnetopause model with  
 266 Cassini's KSM position at the crossing times discussed below (see Figure 3 and Table 1).  
 267

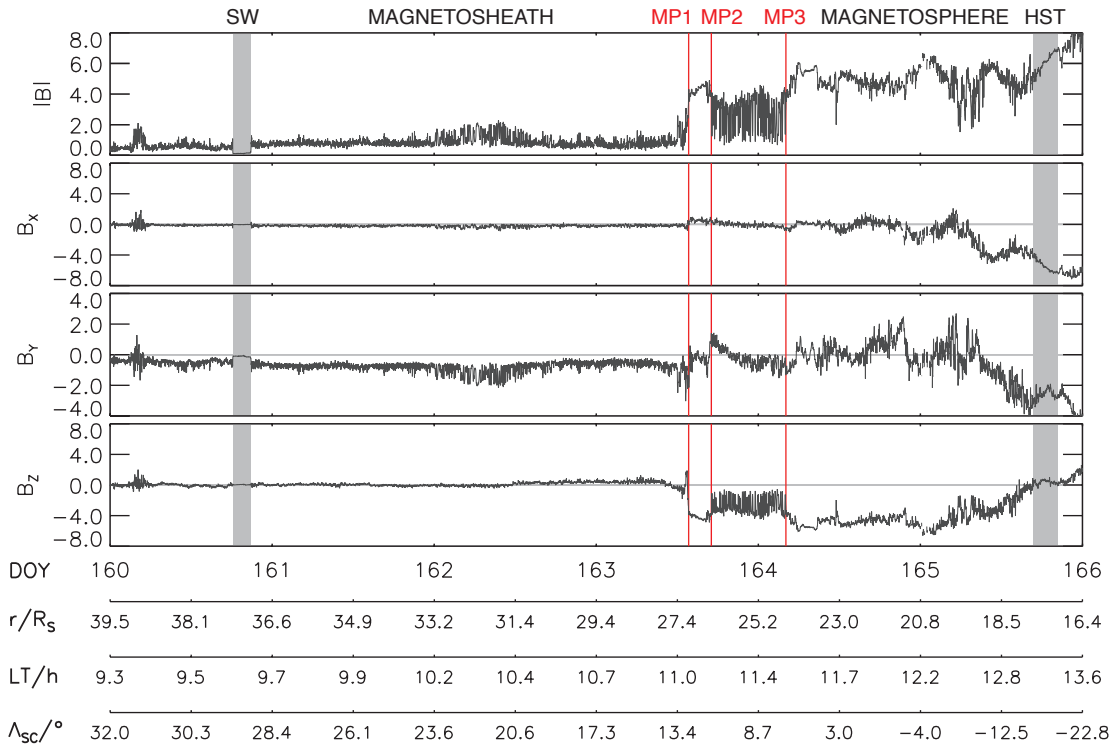


268  
 269

270 Figure 2. Cassini's trajectory during revolution 205 (days 151-184). The left plot shows the  
 271 spacecraft's orbital trace (solid black line) as viewed from above the northern hemisphere in the KSM  
 272 X-Y plane. The right plot shows the orbit trace as viewed from the dawn flank in the KSM X-Z plane.  
 273 The Sun is to the right in each case. The green dot on the trajectory marks Cassini's position during a  
 274 solar wind excursion identified in the MAG instrument data on day 160 (see Figure 3). The blue dots  
 275 show magnetopause crossings also detected in MAG data on days 163-164. The red dot shows the  
 276 spacecraft location at the time of the HST observations on day 165, and black dots show spacecraft  
 277 location at the beginning of the days annotated. Dot-dashed lines mark the magnetopause from the  
 278 Kanani et al. [2010] model at standoff distances of 24 and  $27 R_S$ .  
 279

280 Figure 3 shows Cassini MAG traces between days 160-166. The spacecraft's radial distance from  
 281 planet center ( $r$ ), local time (LT), and sub-satellite latitude of the spacecraft ( $\Lambda_{SC}$ ) are provided as  
 282 additional axes. A solar wind encounter was evident as a reduction in  $|B|$  on day 160 during ~1814-  
 283 2038 UT (Cassini's position at this time is marked by the green dot in Figure 3). The IMF magnitude  
 284 was  $\sim 0.1-0.15$  nT, slightly above the  $\sim 0.05$  nT level estimated by models at the same time, but this  
 285 confirms the persistent low level in the wider context of the model traces (see Figure 1). The transverse  
 286  $B_Y$  component was consistently negative and ranged between  $-0.15$  to  $-0.1$  nT, equivalent to the  
 287 positive  $B_T$  component estimated by the model (also of similar magnitude). The Cassini MAG  
 288 instrument also provides a measure of  $B_Z$  component, which ranged from  $0.0-0.1$  nT during the solar  
 289 wind sample; there is no accurate estimate of this parameter from the projection models for  
 290 comparison. The magnetic measurements from Cassini's solar wind encounter verify the projected  
 291 models for several hours on day 160. The direction of the IMF is also preserved in the magnetosheath,  
 292 and Figure 3 shows that the IMF  $B_Y$  component was consistently negative between the solar wind  
 293 encounter on day 160 up to the magnetopause crossing on day 163. The  $B_Z$  component measured in the  
 294 sheath was mostly positive (up to  $\sim 1.0$  nT) on day 163, before reversing polarity to  $\sim -1.0$  nT just before

295 the magnetopause crossing. It is reasonable to suggest that solar wind conditions varied little in the  
 296 days following the solar wind encounter up to the HST observation period (with the exception of IMF  
 297  $B_z$  polarity), given the wider picture of an apparently stable rarefaction period. Model conditions were  
 298 also optimum at the time in terms of object opposition and data coverage (see Section 2.2). Saturn  
 299 kilometric radio (SKR) emissions measured by the Cassini Radio and Plasma Wave Science (RPWS)  
 300 investigation were extremely low throughout days 160-166 (not shown here), although we note the  
 301 presence of a single low-power, low-frequency extension (LFE) on day 162. Strong LFE signatures  
 302 have been linked with the arrival of solar wind compressions at Saturn [Badman et al., 2008], and in  
 303 this case may be associated with the period of magnetosheath field fluctuations of several nT on day  
 304 162 (see Figure 3). This was possibly a short-lived compression region not resolved by the projection  
 305 models.  
 306



307  
 308  
 309 Figure 3. Cassini KSM magnetometer data during days 160-165 of 2014. All y-axes have units of nT.  
 310 A solar wind encounter was evident during ~1814-2038 UT (shaded gray) on day 160 as a reduction in  
 311  $|B|$ , labeled SW. Inbound magnetopause crossings are visible at ~1341 UT on day 163 (red vertical line,  
 312 labeled MP1) and ~0405 UT on day 164 (red line, MP3), with a re-entry into the sheath between these  
 313 two times (MP2). Cassini-planet center distance ( $R_s$ ), local time (LT) position and sub-Cassini latitude  
 314 ( $\Lambda_{sc}$ ) are provided in the additional axes. The HST imaging window on day 165 is also shaded gray  
 315 and labeled HST.  
 316

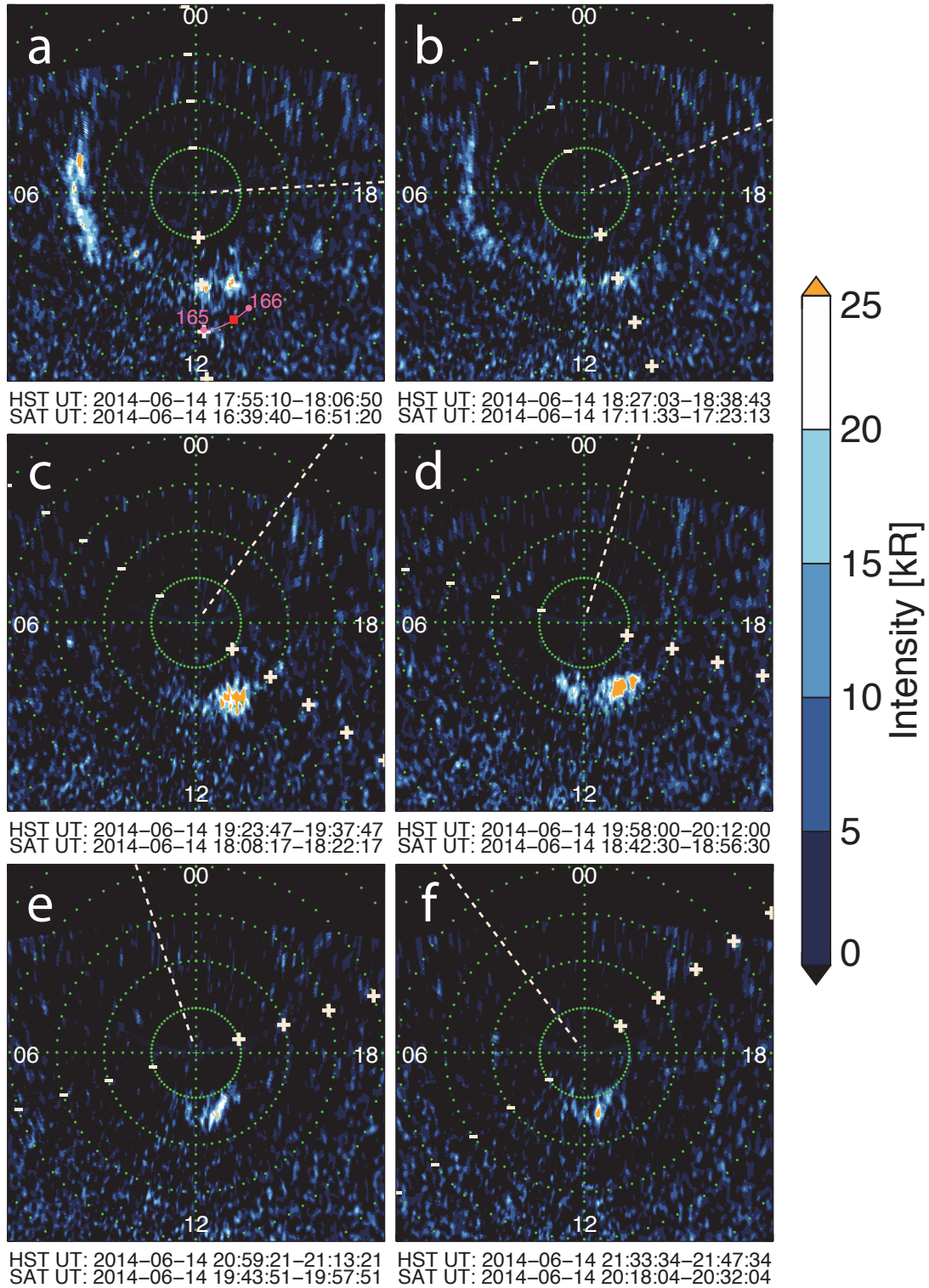
317 Closer to the HST observation window, Cassini crossed the magnetopause inbound at 1341 UT on day  
 318 163 (marked ‘MP1’ in Figure 3). This is evident in Figure 3 as an increase in  $|B|$ , from magnetosheath  
 319 fluctuations below ~2 nT prior to the crossing, to values of ~4-6 nT. Cassini appeared to re-enter the  
 320 magnetosheath between ~1700-0500 UT indicated by the rapid fluctuations of several nT; these ‘dips’  
 321 in magnitude are suggestive of mirror-mode instability structures observed mostly in low- $\beta$  plasma near  
 322 the magnetopause and on the flanks [Cattaneo et al., 1998; Joy et al., 2006]. This outbound  
 323 magnetopause crossing, marked ‘MP2’ in Figure 3 (also vertical red line), suggests the magnetopause  
 324 was compressed beyond the spacecraft before Cassini eventually entered the magnetosphere again at  
 325 0405 UT on day 164 (‘MP3’). We used the magnetopause model of Kanani et al. [2010] (see  
 326 description in Section 2.2) to produce sub-solar magnetopause stand-off distances,  $R_{MP}$ , of ~24-27  $R_s$   
 327 for these two inbound crossings.  
 328

329 A magnetopause standoff distance of ~27  $R_s$  corresponds to an expanded state of the magnetosphere,  
 330 according to the apparent bimodal distribution of standoff distance identified by Achilleos et al. [2008]

331 and more recently Pilkington et al. [2015]; the other state being ‘compressed’ with values of  $\sim 21 R_S$ .  
 332 The range we find therefore, of  $\sim 24-27 R_S$ , indicates that the magnetosphere was closer to a state of  
 333 expansion just a day before the HST observation window. The protracted magnetopause crossing may  
 334 be attributable to a modest compression of an expanded magnetosphere. The corresponding range of  
 335 solar wind dynamic pressure from the Kanani et al. [2010] model for each potential magnetopause  
 336 crossing was 0.0086-0.0143 nPa, compared with the solar wind propagation model values of 0.0017-  
 337 0.0022 nPa at the same time. We discuss this further in Section 4.1.

338  
 339  
 340

### 3.3 HST STIS images



341  
 342

343 Figure 4. A sequence of HST STIS images of Saturn’s northern FUV aurora (SrF2 filtered) in  
344 stereographic projection. Local noon is fixed at the bottom of each image. The sequence spans times  
345 16:39:40 to 20:32:04 Saturn UT on day 165 of 2014. Time between images varies, with image start and  
346 end times labeled under each exposure in HST UT and light travel time-corrected time at Saturn,  
347 labeled ‘SAT UT’. Green dots show points of  $1^\circ$  latitude at intervals of  $90^\circ$  longitude, and points of  $5^\circ$   
348 grid longitude at intervals of  $5^\circ$  latitude from the pole. White dashed lines mark the local time position  
349 of the model Provan et al. [2016] northern PPO current system effective dipole, with associated  
350 maximum upward and downward current regions shown as plus and minus symbols. The pink trace on  
351 image 4a shows Cassini’s ionospheric footprint on day 165, as described in the text. The red square  
352 marks Cassini’s footprint at the mid-exposure time of image 4a.  
353

354 Figure 4 shows a sequence of six HST STIS images of Saturn’s northern auroral region, captured on  
355 three HST orbits between 1755-2148 UT on day 165; together they form the main focal point of this  
356 study. Labeled underneath each image 4a-f is both the HST exposure time stamp (start-end time) and  
357 light-travel corrected time stamp at Saturn (‘SAT UT’), ranging from 1755-2148 UT and 1640-2032  
358 UT respectively. The images are stereographic projections produced using the pipeline summarized in  
359 Section 2.1, and are rotated such that local noon is at the bottom of each image, with dawn to the left  
360 and dusk to the right. The black area at the top of each image (night-side) is the result of cropping out  
361 distorted pixels at the far limb following projection onto the spheroid. A sub-Earth latitude of  $\sim 22^\circ$   
362 subtended at Saturn allowed HST to observe the main auroral emission latitudes across the whole local  
363 time range, including the nightside region as Saturn enters its northern spring season. Based on the  
364 latest model values from Provan et al. [2016], the expected local time angle of the maximum upward  
365 FAC associated with the northern PPO rotating current system is shown by white plus symbols (6 hrs  
366 behind the northern PPO dipole). White dash symbols show the expected local time angle of the  
367 maximum downward FAC associated with the northern PPO systems. Dashed white lines show the  
368 local time angle of the northern effective dipole. The pink trace on Figure 4a marks the ionospheric  
369 footprint of Cassini during day 165, mapped using the Burton et al. [2010] planetary field model,  
370 modified by a ring current contribution for an expanded magnetosphere with standoff distance of  $26 R_S$   
371 [Bunce et al., 2008]; this model does not include effects from the magnetopause or tail currents and  
372 therefore is most accurate sufficiently inside the magnetopause (within  $\sim 15$ - $16 R_S$ ). Figure 3 shows that  
373 Cassini was located in the IMF and magnetosheath prior to  $\sim$  midday on day 163, hence we use the  
374 Bunce et al. [2008] model to approximate Cassini’s footprint on day 165 only.  
375

376 The earliest image in the sequence, Figure 4a (1640-1651 Saturn UT), shows an auroral morphology  
377 with two main features. A dawn arc emission extended between  $\sim 3$ - $9$  local time (LT) with colatitude  
378 extent of  $\sim 5$ - $11^\circ$  and intensities of up to  $\sim 30$  kR. Also visible is an area of emission located between  
379  $\sim 9$ - $13^\circ$  colatitude and  $\sim 11$ - $14$  LT. This area possibly consisted of two separate spot structures separated  
380 in local time by only tens of minutes (two orange spots near noon in Figure 4a), but in the presence of  
381 image noise and with a lack of prior imagery to observe temporal development, this is unclear. The  
382 morphology in Figure 4a persisted in Figure 4b (1712-1723 Saturn UT), but with a marked decrease in  
383 intensity of both dawn arc and post-noon emissions to levels below  $\sim 20$  kR. The dawn arc remained  
384 fixed in terms of colatitude at  $\sim 13^\circ$ , but its latitudinal width decreased by several degrees, extending  
385 between  $\sim 9$ - $13^\circ$  (see extents of the dawn arc structure shown at 1712 UT in Figure 5a). The post-noon  
386 emission area faded to an intensity level just perceptible above the background, but remained fixed in  
387 local time.  
388

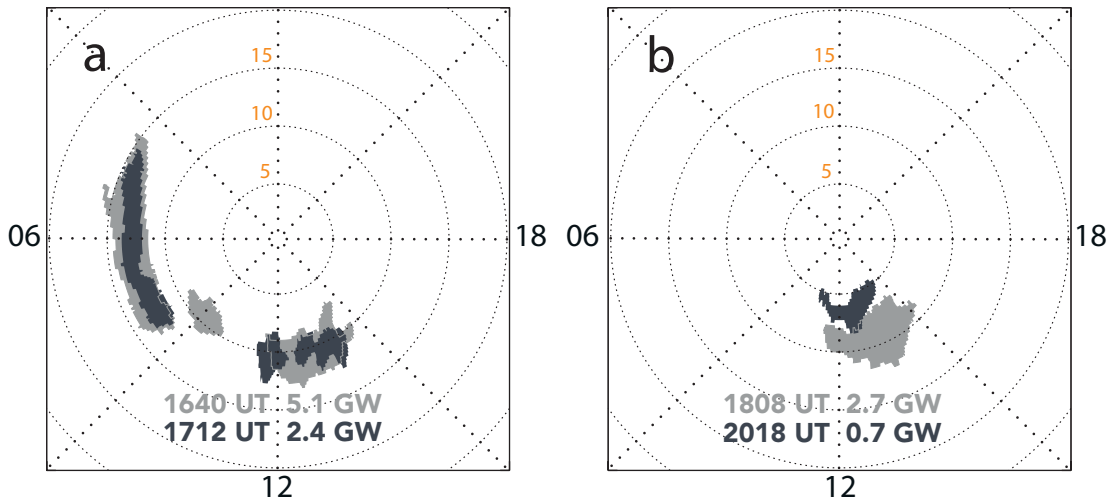
389 The four subsequent images in Figure 4 (4c-f) clearly show a different morphology. The dawn arc  
390 emission, present in Figures 4a and 4b, had evidently faded to a level below the limit of detectability by  
391  $\sim 1808$  UT and remained absent throughout the rest of the observation window. Indeed the only  
392 emissions detected in the rest of the sequence constituted an isolated spot feature fixed in local time  
393 around noon, which may have been a reappearance of the noon spots in the previous two images.  
394 Visible in each of the Figures 4c-f, the spot was brightest in Figure 4d (1843-1857 Saturn UT) with a  
395 peak intensity of 49 kR.  
396

397 In order to track the spatial and temporal development of this feature (and that of the earlier dawn arc  
398 and noon emissions), we applied several image processing steps to systematically quantify the spot’s  
399 area and intensity. A second motivation for this was to extract an estimate of emitted auroral power  
400 from the separate emission structures. The corresponding non-projected images of those in Figure 4  
401 were firstly smoothed using a 7-pixel boxcar average, then regions of interest defined as the pixels  
402 where intensity  $> 3$  kR. The total emitted power (see Table 2) was calculated as the multiple of total

403 pixel count rate with the squared HST-Saturn distance (at the time of exposure) and a conversion factor  
 404 of  $9.04 \times 10^{-10}$  [after Gustin et al. 2012].  
 405

406 Results of the above procedure are shown by the two stereographic projections in Figure 5. The shaded  
 407 areas represent the re-projected regions of interest identified by the tracking procedure. Figure 5a  
 408 depicts the dawn arc and post-noon emission morphology of images shown in Figure 4a (1640 UT,  
 409 light gray) and Figure 4b (1712 UT, dark gray). Figure 5b depicts the extents of the isolated spot  
 410 feature of Figure 4c (1808 UT, light gray) and Figure 4f (2018 UT, dark gray) i.e. the earliest and latest  
 411 images in which the spot constituted Saturn’s entire auroral emission in Figure 4. The total auroral  
 412 power emitted at each time is annotated in the matching gray shade. We omit the 1842 UT (Figure 4d)  
 413 and 1943 UT (Figure 4e) morphologies in Figure 5b for clarity, but area extents and power values of  
 414 the isolated spot are listed in Table 1.  
 415

416 Together, Figure 5 and Table 1 quantify the basic development of the auroral morphology and power  
 417 output during the HST observation window. We note that the simple image processing steps here may  
 418 not be as effective in the tracking and separation of more complex auroral structure at Saturn. Figure 5a  
 419 clearly shows narrowing of the dawn arc between the two earlier images, together with the patches of  
 420 emission around noon that remain approximately fixed in local time and colatitude. The smaller patch  
 421 of emission at 1640 UT, located poleward of the dawn arc at  $\sim 8$ -10 LT and  $8$ - $11^\circ$ , was detected in only  
 422 one exposure (Figure 4a), nevertheless contributing to the total emitted power of the aurora (above the  
 423 detection threshold) at that time. The estimated total auroral power output reduced by a factor of  $\sim 2$ ,  
 424 from 5.1 GW to 2.4 GW, in  $\sim 30$  minutes between exposures. Looking at Figure 5b we can see that,  
 425 following the disappearance of the dawn arc, the now-isolated spot moved polewards while remaining  
 426 fixed at  $\sim 10$ -15 LT (noting that a small area at high latitude spans a wide local time range). Its  
 427 estimated power output decreased from 2.7 GW to 0.7 GW over  $\sim$  two hours. It is interesting to note  
 428 that the 2.7 GW power output of the isolated spot at 1808 UT was greater than the 2.4 GW emitted by  
 429 the combined auroral forms at 1712 UT.  
 430



431  
 432 Figure 5. Auroral morphology at different times throughout the HST imaging sequence on day 165, in  
 433 fixed local time, polar stereographic projection of Saturn’s northern hemisphere. Degrees of colatitude  
 434 are labeled in orange and marked by  $1^\circ$  black dots at intervals of  $45^\circ$  grid longitude. In each window,  
 435 5a and 5b, the earlier morphology is shaded in light gray, the later in dark gray, with matching  
 436 annotations of image exposure time and total emitted power at that time from all regions. Light gray  
 437 lines outline the earlier morphology when structures overlap between exposures.  
 438  
 439

Table 1. Latitude-Local Time (LT) extents and power of the auroral spot

Image start time (UT)	Max. colatitude ( $^\circ$ )	Min. colatitude ( $^\circ$ )	LT min. (hr)	LT max. (hr)	Power (GW)
16:40	13.0	6.8	11.5	14.7	1.87

17:12 <sup>a</sup>	12.5	8.0	11.2	14.4	1.12
18:08	12.0	6.3	11.3	15.3	2.69
18:43	10.8	5.3	10.0	15.4	3.13
19:44	8.5	4.8	12.2	15.3	0.86
20:18	8.3	4.3	10.6	14.6	0.73

<sup>a</sup>Combined properties of the two dark gray regions around noon at 1712 UT in Figure 5a, considered to be part of the same spot feature here and separated only as a result of the systematic image threshold used to track the features.

Table 1 provides the maximum spatial extents of the isolated spot in each exposure of Figure 4, based on the areas identified through image processing and re-projection to a stereographic grid. After 1808 UT the spot generally reduced in both area and emission power as it moved polewards (this is discussed further in Section 4).

## 4 Discussion

We now consider the cause of the unusual auroral morphology observed by HST on day 165; the fading and eventual absence of the dawn arc and an isolated spot moving to high latitude.

### 4.1 Solar wind conditions & state of magnetosphere

Our interpretation of Saturn’s northern auroral morphology on day 165 depends on the state of both the magnetosphere and incoming solar wind. The solar wind projection models (Section 3.1), complimented by Cassini measurements (Section 3.2), indicate that the HST observations were made following a prolonged period of rarefaction. For two weeks (days 153-165) the radial velocity gradually decreased to below 350 kms<sup>-1</sup>, and the IMF magnitude was consistently < 0.1 nT, in agreement with statistical values associated with rarefaction regions at Saturn [Jackman et al., 2004]. On the two days prior to the HST observations, estimates of dynamic pressure from the solar wind models (Figure 1) and Kanani et al. [2010] model during detected magnetopause crossings (Figure 3) were similarly low, with maximum values of 0.0022 nPa and 0.0143 nPa respectively. The solar wind propagation models also show a period of disturbance developing after day 167 (towards the end of the uncertainty window in Figure 1), and it is possible that the auroral images were taken during the early stages of a compression in the solar wind, in which the projected IMF magnitude and dynamic pressure increased to ~0.2 nT and 0.25 nPa, respectively. However the images show no evidence of the ‘storm’ time morphology associated with strong magnetospheric compression (as reviewed by Meredith et al. [2015]), and we conclude that the auroras observed do not correspond to any significant compression interval.

Based on the two magnetopause crossings of Cassini identified in Figure 3, estimates of the sub-solar standoff distance were obtained using the Kanani et al. [2010] magnetopause surface model (Table 1). Cassini was well positioned to enable this estimate, having crossed the magnetopause close to local noon and at low-latitude just the day before the HST observations (see blue dots in the trajectory plots of Figure 2). The estimated standoff distance reduced from ~27 R<sub>S</sub> to ~24 R<sub>S</sub> in the ~14.5 hrs between resampling the magnetopause, suggesting compression of the magnetosphere beyond the spacecraft during this time. Although the solar wind projections show no evidence of compression transients, the Cassini MAG trace did detect minor fluctuations of the magnetosheath field magnitude on day 162 (Figure 3) associated with a possible low frequency extension in SKR emission. These standoff distance estimates do, however, fall into the expanded or ‘inflated’ end of the bimodal standoff distribution identified statistically by Pilkington et al. [2015], which peaks at ~27 R<sub>S</sub>.

The strongest indication here of an expanded magnetosphere may be the complete disappearance of Saturn’s dawn arc (Figures 4 & 5). A dawn arc is normally present to some degree in this highly rotational system, being driven by field-aligned currents (FACs) located equatorward of (and up to) the OCB, mapping to regions of flow shear or pressure gradients in the outer magnetosphere [Jinks et al., 2014; Belenkaya et al., 2014]. If the magnetosphere expands, the closed, outer field lines are expected

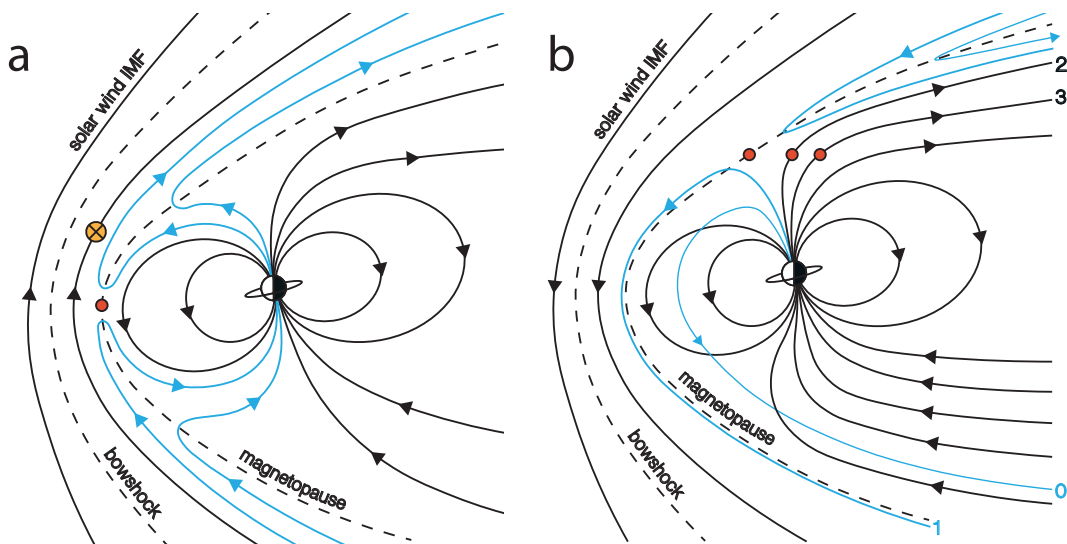
490 to lag even further behind co-rotation as angular momentum is conserved, so that the shear in plasma  
 491 angular velocity between these field lines and those at higher latitudes (including those possibly  
 492 affected by solar wind viscous interactions in the magnetopause boundary layer, or open field lines in  
 493 the polar cap) is reduced on the dawn side. A complete switch-off of Saturn's dawn arc further suggests  
 494 that there is no sunward return flow along the dawn flank from nightside reconnection, which can  
 495 enhance flow shears, pressure gradients, and hot plasma precipitation in this sector [Cowley et al.,  
 496 2005; Grodent et al., 2005; Mitchell et al., 2009; Belenkaya et al., 2014; Badman et al., 2016]. This  
 497 scenario is quite feasible during a period of solar wind rarefaction, nevertheless the complete absence  
 498 of a dawn auroral arc has rarely been observed at Saturn, and in those cases dusk emissions were  
 499 present instead [e.g. Gérard et al., 2006; Nichols et al., 2010; 2016].  
 500

#### 501 4.2 Low latitude dayside reconnection

502  
 503 We now consider the possible dayside reconnection scenarios that may have produced the isolated  
 504 auroral spot signature on day 165, considering its intensity, lack of motion in the corotation direction,  
 505 and clear poleward motion throughout an observed lifetime of at least two hours.  
 506

507 An auroral signature produced by dayside reconnection will appear initially at the OCB, regardless of  
 508 whether the reconnection site is at low or high latitude. The spot observed here appeared at main  
 509 emission latitudes before moving poleward. The first HST image at 1640 UT shows that the median  
 510 colatitude of the noon emission was  $\sim 10^\circ$ , compared with the  $\sim 13^\circ$  of the dawn arc. This is consistent  
 511 with the most recent HST survey of Saturn's northern auroral emissions by Nichols et al. [2015], which  
 512 places the main emission between  $\sim 6.7^\circ$ - $12.5^\circ$  colatitude at noon and  $\sim 13.4^\circ$ - $15.8^\circ$  colatitude at dawn.  
 513 The final image in the HST image at 2018 UT shows that the spot moved polewards and away from the  
 514 main emission region to within  $4.3^\circ$  of the pole itself.  
 515

516 The poleward motion of the spot is consistent with precipitation on a newly-opened field line following  
 517 reconnection at low latitudes, under northward IMF conditions. As illustrated in Figure 6a, the  
 518 magnetic tension and magnetosheath flow act to move newly opened field lines anti-sunwards.  
 519 Meredith et al. [2014] found significant noon-dusk sector auroral patch occurrence during northward  
 520 IMF conditions (based on HST images and Cassini solar wind measurements upstream). This matches  
 521 the initial images of the HST sequence here, including the co-presence of a dawn arc (present  
 522 throughout the Meredith et al. [2014] study, although no clear dependence on IMF direction was  
 523 found). The difference in this case is the fading and disappearance of the dawn arc after 1712 UT,  
 524 simultaneous with the spot signature moving polewards and away from main emission latitudes  
 525 (compare Figure 5a and 5b).  
 526



527  
 528  
 529 Figure 6. Conceptual sketches showing the dayside reconnection process at Saturn, as viewed in the  
 530 day-night meridian with the Sun to the left in each case. Solid black lines with arrows represent solar  
 531 wind and magnetospheric field orientation. Reconnection sites are shown by red dots, where the IMF  
 532 and planetary field lines are antiparallel. Newly reconfigured field lines (following reconnection) are  
 533 shaded blue. Dashed black lines mark the bowshock and magnetopause boundaries. 6a shows the low-

534 latitude case when IMF is northward. The yellow circled cross indicates a negative  $B_Y$  component of  
 535 the IMF as indicated by Cassini measurements and model projections in Section 3. 6b shows the case  
 536 of southward IMF, when draped solar wind flux may reconnect with planetary lobe flux. Field lines  
 537 numbered 0-4 illustrate the circulation of newly reconfigured flux initially sunward (1), and then  
 538 around the flanks with magnetosheath flow (0). Several reconnection sites are shown, indicating the  
 539 successive reconnection with older, open lobe flux (2-3) required to produce poleward motion of an  
 540 auroral signature.  
 541  
 542 Aside from the clear poleward motion of the spot, its position was also fixed in local time between  
 543 ~10-15 LT (the center of the spot was fixed at ~1330 LT, see Table 1). If the dayside aurora were being  
 544 driven by low-latitude reconnection, prior studies suggest that we may expect some evidence of sub-  
 545 corotation of auroral signatures, or at least their equatorward extent [e.g. Radioti et al., 2013]. Meredith  
 546 et al. [2014] report high-latitude emissions within the noon-dusk sector during northward IMF  
 547 conditions that may be bifurcation structures at spatial scales not fully resolvable by the HST STIS.  
 548 Bifurcations of the main emission region were observed more clearly by Radioti et al. [2011] and  
 549 Badman et al. [2013] using the Cassini Ultra Violet Imaging Spectrograph (UVIS), and were associated  
 550 with high dynamic pressure in the solar wind and subsequent magnetospheric compression. However  
 551 the solar wind appears to have been in rarefaction during day 165 (see Section 4.1), and we see no  
 552 evidence of rotation or bifurcation of the auroral emissions. Considering the polarity of Saturn's  
 553 magnetospheric dipole and magnetic tension forces following reconnection with the IMF, a dawnward  
 554 transverse IMF component (negative  $B_Y$  in the KSM frame, positive  $B_T$  in RTN) may restrict  
 555 corotational motion of a newly opened field line in the northern dayside ionosphere [Bunce et al.,  
 556 2005] as suggested by the annotation in Figure 6a. This is supported by the steady polarity of the IMF  
 557 model estimates (positive  $B_T$ ), the in situ Cassini IMF measurement on day 160 (negative  $B_Y$ ), and the  
 558 IMF polarity retained in the magnetosheath field measured by Cassini in the days leading up to the  
 559 magnetopause crossing (negative  $B_Y$ ). It is feasible that a significant transverse component of the IMF  
 560 'held back' the auroral signature against corotation, resulting in the fixed local time position observed.  
 561  
 562 In addition to poleward motion, the UV intensity (up to 49 kR) and longevity (> 2 hrs) of the spot  
 563 signature are particularly notable. It is clear from Figures 4c-d that the spot was more intense in the  
 564 early stages of its lifetime, before dimming as it moved poleward over several hours. Note also the  
 565 reduction in both size and UV power emission of the signature detailed in Table 1. We suggest that this  
 566 is consistent with the convection of recently opened flux over the polar cap following reconnection at  
 567 low latitude (as illustrated in Figure 6a); the reduction in emission power being proportional to the  
 568 gradual depletion of any source particle population trapped on the convecting field line. Without  
 569 particle measurements from Cassini this remains an interpretation, but we may now compare our  
 570 observation with the expected emission power of an auroral cusp signature driven by low-latitude  
 571 reconnection.  
 572  
 573 The model of Bunce et al. [2005] simulates the IMF control of Saturn's polar cusp aurora. Using  
 574 typical electron population sources in the outer magnetosphere, plasma mantle and lobe magnetosheath  
 575 regions, Knight theory [1973] is used to derive the field-aligned voltages required to drive UV auroral  
 576 emission through pulsed dayside reconnection at low and high latitude mapping positions, for varying  
 577 IMF  $B_Y$  polarity. Table 2 compares the emission intensity and power of the spot observed here with  
 578 Bunce et al. [2005] model estimates for 'slow flow' solar wind conditions (applicable to periods of  
 579 rarefaction and pertinent here). For simplicity, we quote only the upper model estimates of mean ( $\langle I \rangle$ )  
 580 and maximum ( $I_{MAX}$ ) emission intensities, independent of the IMF  $B_Y$  orientation or source population  
 581 provided by the Bunce et al. [2005] model, together with ranges of total emitted UV power for the low  
 582 latitude and high latitude case. Also listed in Table 2 are modeled and observed (values in brackets)  
 583 parameters of polar cusp emissions at Saturn reported by Gérard et al. [2005], a study that adapted the  
 584 Bunce et al. [2005] model to match observations made by HST. Gérard et al. [2005] found that  
 585 significant increases of reconnection voltage and ionospheric flow speeds were required to bring the  
 586 Bunce et al. [2005] estimates of UV intensity and power close to those observed by HST; suggesting  
 587 that the lobe reconnection process may be more efficient at Saturn than predicted by the model. The  
 588 lobe reconnection potential used in the Bunce et al. [2005] model was assumed to be half of that for  
 589 low latitude reconnection, based on the terrestrial study of Milan et al. [2004]. We attempt no such  
 590 tailored comparison with the model here, noting only that the reconnection voltage of 200 kV proposed  
 591 by Gérard et al. [2005] is more typically associated with compression-related levels on the dayside  
 592 [Jackman et al., 2004], but here we have several indicators that the magnetosphere was not compressed  
 593 (see Section 4.1).

594  
595  
596  
597  
598  
599  
600  
601  
602  
603  
604  
605  
606  
607  
608  
609  
610  
611  
612  
613  
614  
615  
616  
617  
618  
619

In Table 2 we provide the total UV power per nominal emission area of  $10^{12} \text{ m}^2$ , thereby accounting for the different areas of the cusp signature reported by the Bunce et al. [2005] and Gérard et al. [2005] studies. The spot area quoted in Table 3 for this study ( $1.6 \times 10^{12} \text{ m}^2$ ) was calculated using the LT and latitude extents at 1843 UT in Table 2 and an approximation of 1000 km subtended per degree in the image. The total emitted power per area of the day 165 spot ranged between 0.46-1.96  $\text{GW}/10^{12} \text{ m}^2$ . Considering the low-latitude reconnection values (high latitude reconnection is discussed in Section 4.3), this is closer in magnitude to the adapted model estimate of Gérard et al. [2005], at 0.22-1.27  $\text{GW}/10^{12} \text{ m}^2$ , than the equivalent Bunce et al. [2005] estimate of 0.03-0.52  $\text{GW}/10^{12} \text{ m}^2$  (particularly the upper end of the ranges). We note that the Gérard et al. [2005] study calculated emission power using the STIS UV bandwidth of 115-170 nm i.e. not extrapolated over the unabsorbed wavelength range of  $\text{H}_2$  emissions as per the Gustin et al. [2012] method used in this study. We therefore expect the Gérard et al. [2005] power values to be lower relative to those of this study by a factor of  $\sim 2$  (factor for converting observed count rate to total unabsorbed  $\text{H}_2$ , divided by image exposure time). Taking this into account, the Gérard et al. [2005] observed value of 0.42  $\text{GW}/10^{12} \text{ m}^2$  becomes a comparable 0.84  $\text{GW}/10^{12} \text{ m}^2$ . The maximum emitted power of the spot reported here was 1.96  $\text{GW}/10^{12} \text{ m}^2$ , confirming that it appears to have been more powerful per unit area than the Bunce et al. [2005] model predictions and previous cusp emissions observed with HST, but comparable with the adapted low-latitude model case by Gérard et al. [2005] (up to 2.54  $\text{GW}/10^{12} \text{ m}^2$ ). The comparisons in Table 2 are not direct, and the Bunce et al. [2005] model appears to underestimate the efficiency of dayside reconnection in producing auroral emissions as suggested by Gérard et al. [2005]; we include Table 2 as a summary review of similar case studies.

Table 2. Auroral cusp spot parameters from the conceptual ‘slow flow’ model of Bunce et al. [2005] compared with the adapted model results and observations of Gérard et al. [2005] and the brightest spot imaged in this study.

Study	Reconnection location	Area ( $\text{m}^2$ )	$\langle I \rangle$ (kR)	$I_{\text{MAX}}$ (kR)	Power (GW)	Power per unit area ( $\text{GW} / 10^{12} \text{ m}^2$ )
Bunce 2005	High latitude	$0.3 \times 10^{12}$	11.2	41.0	0.00-0.17	0.00-0.55
Bunce 2005	Low latitude	$2.1 \times 10^{12}$	25.6	193.9	0.07-1.10	0.03-0.52
Gérard 2005	High latitude	$8.0 \times 10^{12}$	0.7-25.4 (21.0) <sup>a</sup>	-	0.06-2.20 (5.0) <sup>a</sup>	0.00-0.28 (0.63) <sup>a</sup>
Gérard 2005	Low latitude	$6.0 \times 10^{12}$	18.4- 105.5 (20.0) <sup>a</sup>	-	1.3-7.6 (2.5) <sup>a</sup>	0.22-1.27 (0.42) <sup>a</sup>
This study	?	$1.6 \times 10^{12}$	11.1	49.0	0.73-3.13	0.46-1.96

<sup>a</sup>HST observed parameters from the Gérard et al. [2005] study.

620  
621  
622  
623  
624  
625  
626  
627  
628  
629  
630  
631  
632  
633  
634  
635  
636  
637  
638  
639

#### 4.3 High latitude dayside reconnection

The auroral spot was located at high latitudes toward the end of the HST image sequence, with a poleward extent of only  $4^\circ$  colatitude (see Table 1). We consider here whether reconnection between the solar wind and planetary lobe flux could have driven the isolated spot emission. At Saturn this is more likely when upstream IMF is orientated southward, and the antiparallel reconnection site shifts away from low latitudes where the planetary field is also southward. Draped solar wind flux then reconnects with open lobe flux, and is re-circulated – initially equatorward - around the flanks in the direction of magnetosheath flow. Because no new open flux is produced, the overall OCB position remains unchanged; this process has been referred to as ‘lobe stirring’ [e.g. Reiff, 1982; Crooker, 1992; Bunce et al., 2005]. We cannot say if this process was occurring in the southern hemisphere, although dual-hemispheric lobe reconnection is unlikely at Saturn due to the requirement for simultaneous and conjugate reconnection in each hemisphere [Cowley et al., 2008]. If this were the case, we would expect the aurora to appear initially just poleward of the OCB, before relaxing equatorward as the OCB reconfigures when open flux is closed. Terrestrial studies suggest that the lobe region is more susceptible to reconnection with draped IMF in the summer hemisphere, with a dependence on the IMF  $B_x$  component [e.g. Crooker & Rich, 1993; Lockwood and Moen, 1999; Fear et al. 2015]; here we observed Saturn’s northern hemisphere in spring, with a planetary axial tilt of  $\sim 22^\circ$ .

640  
641 How do we resolve the clear poleward motion of the spot if it was driven by lobe reconnection?  
642 Following single lobe reconnection, magnetic tension force is expected to initially contract the newly  
643 reconfigured open field line in a sunward direction, as it now threads the dayside magnetopause (e.g.  
644 see the terrestrial descriptions of Reiff [1982] or Lockwood & Moen [1999]). The particles undergoing  
645 auroral acceleration along this field line would therefore map as a signature with equatorward motion  
646 within the dayside cusp region of the ionosphere [e.g. Milan et al., 2000b], although any equatorward  
647 motion may be limited by the OCB position remaining effectively unchanged. Over a longer time scale,  
648 however, prolonged dayside lobe reconnection could successively reorder more poleward open lobe  
649 flux [e.g. Doss et al., 2015], resulting in an auroral signature that moves polewards from the OCB as  
650 observed here. Figure 6b provides a hypothetical sketch of this process, with red dots illustrating the  
651 multiple reconnection sites. We note, however, that the total emitted power of the spot reduced by a  
652 factor of 3-4 throughout its > 2 h lifetime (attributed to both a decrease in the size of the spot and its  
653 brightness, see Table 1), whereas in the case of ongoing reconnection with magnetosheath field lines,  
654 we may expect the auroral spot to maintain a more stable brightness level if the source magnetosheath  
655 particle population was providing a relatively unchanged energy flux over two hours.

656  
657 It is possible for a strong IMF  $B_Y$  component to prevent the expected equatorward and duskward  
658 motion of the cusp spot resulting from a pulse of lobe reconnection, while precipitation of the  
659 accelerated plasma continues for several hours [Bunce et al., 2005; Cowley et al., 2005; Meredith et al.,  
660 2013]. We have already proposed that incidence of negative IMF  $B_Y$  fixed the spot emission in local  
661 time within the low-latitude reconnection scenario of Section 4.2, but such IMF orientation would  
662 equally affect the motion of open flux at high latitude (see the terrestrial case of Milan et al. 2000b);  
663 potentially more-so since the plasma rotation effects evident in open flux production at the equator (e.g.  
664 sub-corotation of auroral bifurcations [Radioti et al., 2011; Badman et al., 2013]) are not expected to be  
665 as dominant towards high latitudes [Cowley & Bunce, 2003; Stallard et al., 2004]. Meredith et al.  
666 [2014] attributed a high-latitude FUV emission in Saturn's northern aurora as a lobe signature  
667 (reaching up to the pole itself), supported by measurement of the incident southward IMF upstream by  
668 Cassini and a magnetic field model mapping the emission to open field lines [Belenkaya et al., 2014].  
669 Meredith et al. [2014] also cited lack of corotation of the high latitude spot being consistent with lobe  
670 reconnection.

671  
672 We can again compare to the results of Bunce et al. [2005] and Gérard et al. [2005] shown in Table 2.  
673 The closest UV emission power compared to the spot observed here ( $0.46-1.96 \text{ GW}/10^{12} \text{ m}^2$ ) is that of  
674 the high-latitude cusp emission observed by Gérard et al. [2005], which emitted  $1.26 \text{ GW}/10^{12} \text{ m}^2$ ,  
675 noting the factor  $\sim 2$  adjustment for UV filter bandwidth discussed in Section 4.1. Note that the  
676 emission area quoted from the Gérard et al. [2005] study ( $8.0 \times 10^{12} \text{ m}^2$  for the high-latitude case)  
677 combines the Bunce et al. [2005] model region equatorward and poleward of the OCB, and therefore  
678 the plasma mantle and magnetosheath source populations. The high reconnection voltages required to  
679 produce the Gérard et al. [2005] model estimates may also be excessive during periods of rarefaction as  
680 discussed previously.

#### 681 682 4.4 Effect of planetary period rotating current systems 683

684 Some element of the auroral spot's poleward motion could be attributed to the  $\sim \pm 1^\circ$  planetary period  
685 oscillation (PPO) of the entire northern oval position. This oval oscillation has been seen repeatedly in  
686 HST imagery from both hemispheres [Nichols et al. 2008; 2010; 2016]. The auroral oval is expected to  
687 be displaced equatorward in the direction of a region of rotating maximum upward PPO current [Hunt  
688 et al., 2015; Badman et al., 2016]. Indeed, modulation of the position of the southern cusp, associated  
689 with the PPO, has recently been observed in situ with Cassini [Arridge et al., 2016].

690  
691 The spot intensity on day 165 appeared to increase (by at least a factor of two) as the expected  
692 maximum northern PPO upward current rotated through the region, evident from the white crosses in  
693 Figures 4b-c (see the caption of Figure 4 for a description of PPO current annotation). If the upward  
694 rotating current sector were modulating the spot intensity, we expect an increase in emission intensity,  
695 at least toward main emission latitudes where the PPO currents map. In terms of position, however, the  
696 expected oval oscillation would have shifted the upward FAC region equatorward and not poleward at  
697 this time. We note that the oval  $1-2^\circ$  oscillation magnitude occurs over a planetary period of  $\sim 10-11$   
698 hours; here we observe a median poleward motion of  $\sim 4^\circ$  in just two hours. The possible modulation of  
699 the spot intensity by the northern PPO current system is notable, but oscillation of the oval associated

700 with the PPOs does not appear to account for its movement towards the pole. It is also possible that the  
701 PPO systems could modulate magnetopause processes [e.g. Clarke et al., 2006], however the PPO  
702 currents discussed here flow at main emission latitudes [e.g. Hunt et al., 2015], and the emission spot  
703 observed reaches notably higher latitudes i.e. likely on open field lines.

704

## 705 5 Summary

706

707 We have examined a case of unusual UV auroral morphology in Saturn's northern hemisphere,  
708 observed by the HST STIS instrument on 14 June 2014 (day 165). The fading and eventual  
709 disappearance of the dawn arc was followed by the formation of an isolated and persistent high latitude  
710 spot emission at post-noon local time. Present for at least two hours, the spot moved polewards by a  
711 median  $\sim 4^\circ$  latitude to a minimum colatitude of  $\sim 4^\circ$ , remaining fixed in local time and displaying  
712 intensities of up to 49 kR. We systematically tracked the dawn arc and spot areas using image  
713 smoothing and intensity threshold contouring of un-projected images, allowing an estimate of emitted  
714 power to be made using the method of Gustin et al. [2012]. The maximum total emitted power of the  
715 isolated spot was 3.13 GW (corresponding to an area of  $\sim 1.6 \times 10^{12} \text{ m}^2$ ), which is significant considering  
716 the total auroral morphology emitted between 2.4-5.1 GW prior to the disappearance of the dawn arc.

717

718 Complete absence of the dawn arc is rarely observed at Saturn [e.g. Gérard et al., 2006]. Cassini  
719 crossed the magnetopause a few days prior to the observation window at an approximate sub-solar  
720 standoff distance of between 24-27  $R_S$ , indicating an expanded magnetosphere. A period of prolonged  
721 solar wind rarefaction was also indicated by in situ Cassini measurements and model projections from  
722 1 AU. It is likely that the combination of an expanded magnetosphere and quiet solar wind led to the  
723 'switching off' of Saturn's dawn arc, through suppression of the rotational flow shear in the outer  
724 magnetosphere, in the absence of significant night-side reconnection- or plasma injection-driven  
725 sunward flow along the dawn flank. We note that this is different from the behavior of Jupiter's main  
726 auroral oval, which is driven by corotation-enforcement currents in the middle magnetosphere [Cowley  
727 & Bunce, 2001], and is present under all solar wind conditions [Clarke et al., 2009; Nichols et al.,  
728 2009].

729

730 In this context we considered the potential reconnection scenarios that may have driven the isolated  
731 spot emission. The high latitude of the spot is consistent with either lobe or low-latitude reconnection,  
732 whereas its poleward motion is more easily explained by the relaxation of newly opened flux away  
733 from the OCB following low-latitude reconnection. The persistence of the spot for at least two hours  
734 may put a useful lower time constraint on this convection process at Saturn. Given the particularly high  
735 latitude of the emission we also considered the case for successive lobe reconnection at the far lobe  
736 driving the poleward motion, but the availability of a particle population source on older, open flux  
737 required to drive such a persistent emission is questionable. Comparison with previous modeled and  
738 observed polar cusp emissions from two studies, Bunce et al. [2005] and Gérard et al. [2005],  
739 confirmed that the observed spot was indeed a bright cusp emission signature, and perhaps closer to  
740 expectations for low-latitude reconnection driving rather than lobe reconnection, but the distinction is  
741 not clear.

742

743 The spot's fixed LT position may be attributed to negative IMF  $B_Y$  conditions incident at the time,  
744 combined with increased sub-corotation of open flux towards higher latitudes. The emission intensity  
745 was also possibly enhanced by a sector of upward PPO current rotating through the region. These  
746 observations show conclusively that the mechanisms producing noon auroral spots and the 'main oval'  
747 auroras (i.e. the dawn arc) are distinct, since in this case the cusp spot occurred without the arc. This  
748 finding thus supports in an independent way the previous inferences of Radioti et al. [2011], Badman et  
749 al. [2013], and Meredith et al. [2014]. These observations also suggest that reconnection can occur at  
750 an expanded magnetosphere, in agreement with the cusp observations of Arridge et al. [2016], who  
751 found evidence of reconnection under a range of upstream solar wind conditions.

752

753 Prolonged periods of rarefaction are expected during the declining phase of the current solar cycle. The  
754 unusual auroral morphology presented here, captured during what was likely a particularly quiet period  
755 of rarefaction, may be relevant in comparisons with any quieter auroral images obtained during the  
756 upcoming Cassini Grande Finale mission and its inclined orbits over Saturn's polar regions.

757

758 6 Acknowledgements

759

760

761 This work is based on observations made with the NASA/ESA Hubble Space Telescope (observation  
762 ID: GO13396), obtained at the Space Telescope Science Institute (STScI), which is operated by  
763 AURA, Inc., for NASA. The Hubble observations are available from the STScI website. JK, SVB and  
764 AG were supported by STFC grant ST/M001059/1. SVB was also supported by an STFC Ernest  
765 Rutherford Fellowship ST/M005534/1. RLG was supported by an STFC studentship. EJB, GP, HM,  
766 and SWHC were supported by STFC Consolidated Grant ST/N000749/1. JDN was supported by STFC  
767 Advanced Fellowship ST/1004084/1. We thank the Cassini MAG team at Imperial College London for  
768 access to processed magnetometer data, which are available online from the NASA PDS PPI node, and  
769 Bill Kurth (University of Iowa) for providing a description of the RPWS observations. The OMNI data  
770 were obtained from the GSFC/SPDF OMNIWeb interface at <http://omniweb.gsfc.nasa.gov>, and we  
771 thank K.C. Hansen and B. Zieger for providing solar wind propagations from their Michigan Solar  
772 Wind Model (<http://mswim.engin.umich.edu/>). Solar wind model projections from the Tao et al. [2005]  
773 model are available on request from C. Tao.

774 7 References

775

776 Arridge, C. S., et al. (2016), Cassini observations of Saturn's southern polar cusp, *J. Geophys. Res.*  
777 *Space Physics*, 121, 300613030, doi:10.1002/2015JA021957.  
778 Badman, S. V., et al. (2012), Rotational modulation and local time dependence of Saturn's infrared  
779 H3+ auroral intensity, *J. Geophys. Res.*, 117, A09228, doi:10.1029/2012JA017990.  
780 Badman, S. V., A. Masters, H. Hasegawa, M. Fujimoto, A. Radioti, D. Grodent, N. Sergis, M. K.  
781 Dougherty, and A. J. Coates (2013), Bursty magnetic reconnection at Saturn's magnetopause, *Geophys.*  
782 *Res. Lett.*, 40, 1027-1031, doi:10.1002/grl.50199.  
783 Badman, S.V., G. Provan, E.J. Bunce, D.G. Mitchell, H. Melin, J.D. Nichols, S.L. Jinks, S.W.H.  
784 Cowley, T. Stallard, A. Radioti, W.R. Pryor, W.S. Kurth, R.H. Brown, K.H. Baines, M.K. Dougherty  
785 (2016), Saturn's auroral morphology and field-aligned currents during a solar wind compression,  
786 *Icarus*, 263, 83-93, doi:10.1016/j.icarus.2014.11.014.  
787 Belenkaya, E. S., S. W. H. Cowley, C. J. Meredith, J. D. Nichols, V. V. Kalegaev, I. I. Alexeev, O. G.  
788 Barinov, W. O. Barinova, and M. S. Blokhina (2014), Magnetospheric magnetic field modelling for the  
789 2011 and 2012 HST Saturn aurora campaigns - implications for auroral source regions. *Ann. Geophys.*,  
790 6, 689-704, doi:10.5194/angeo-32-689-2014.  
791 Bunce, E. J., S. W. H. Cowley, and S. E. Milan (2005), Interplanetary magnetic field control of  
792 Saturn's polar cusp aurora, *Ann. Geophys.*, 23, 1405-1431, doi:10.5194/angeo-23-1405-2005.  
793 Bunce, E.J., C.S. Arridge, S.W.H. Cowley, and M.K. Dougherty (2008), Magnetic field structure of  
794 Saturn's dayside magnetosphere and its mapping to the ionosphere: Results from ring current modeling,  
795 *J. Geophys. Res.*, 113, A022027, doi:10.1029/2007JA012538.  
796 Burton, M. E., M. K. Dougherty, and C. T. Russell (2010), Saturn's internal planetary magnetic field,  
797 *Geophys. Res. Lett.*, 37, L24105, doi:10.1029/2010GL045148.  
798 Cattaneo, M. B. B., C. Basile, G. Moreno, and J. D. Richardson (1998), Evolution of mirror structures  
799 in the magnetosheath of Saturn from the bow shock to the magnetopause, *J. Geophys. Res.*, 103(A6),  
800 11961-11972, doi:10.1029/97JA03683.  
801 Clarke, J. T., J.-C. Gérard, D. Grodent, S. Wannawichian, J. Gustin, J. Connerney, F. Crary, M.  
802 Dougherty, W. Kurth, S. W. H. Cowley, E. J. Bunce, T. Hill, and J. Kim (2005), Morphological  
803 differences between Saturn's ultraviolet aurorae and those of Earth and Jupiter, *Nature*, 433, 717-719,  
804 doi:10.1038/nature03331.  
805 Clarke, J. T., et al. (2009), Response of Jupiter's and Saturn's auroral activity to the solar wind, *J.*  
806 *Geophys. Res.*, 114, A05210, doi:10.1029/2008JA013694.  
807 Clarke, K. E., et al. (2006), Cassini observations of planetary-period oscillations of Saturn's  
808 magnetopause, *Geophys. Res. Lett.*, 33, L23104, doi:10.1029/2006GL027821.  
809 Cowley, S.W.H., and E.J. Bunce (2001), Origin of the main auroral oval in Jupiter's coupled  
810 magnetosphere-ionosphere system, *Planetary and Space Science*, 49 (10-11), 1067-1088,  
811 doi:10.1016/S0032-0633(00)00167-7.  
812 Cowley, S. W. H., and E. J. Bunce (2003), Corotation-driven magnetosphere-ionosphere coupling  
813 currents in Saturn's magnetosphere and their relation to the auroras, *Ann. Geophys.*, 21, 1691-1707,  
814 doi:10.5194/angeo-21-1691-2003.  
815 Cowley, S. W. H., E. J. Bunce, and R. Prangé (2004), Saturn's polar ionospheric flows and their  
816 relation to the main auroral oval, *Ann. Geophys.*, 22, 1379-1394, doi:10.5194/angeo-22-1379-2004.  
817 Cowley, S. W. H., S. V. Badman, E. J. Bunce, J. T. Clarke, J.-C. Gérard, D. Grodent, C. M. Jackman,

818 S. E. Milan, and T. K. Yeoman (2005), Reconnection in a rotation-dominated magnetosphere and its  
819 relation to Saturn's auroral dynamics, *J. Geophys. Res.*, 110, A02201, doi:10.1029/2004JA010796.  
820 Crary, F. J., et al., 2005, Solar wind dynamic pressure and electric field as the main factors controlling  
821 Saturn's aurorae, *Nature*, 433, 720-722, doi:10.1038/nature03333.  
822 Crooker, N. U. (1992), Reverse convection, *J. Geophys. Res.*, 97 (A12), 19,363-19,372,  
823 doi:10.1029/92JA01532.  
824 Crooker, N. U., and F. J. Rich (1993), Lobe cell convection as a summer phenomenon, *J. Geophys.*  
825 *Res.*, 98(A8), 13403-13407, doi:10.1029/93JA01037.  
826 Desroche, M., F. Bagenal, P. A. Delamere, and N. Erkaev (2013), Conditions at the magnetopause of  
827 Saturn and implications for the solar wind interaction, *J. Geophys. Res. Space Physics*, 118, 3087–  
828 3095, doi:10.1002/jgra.50294.  
829 Doss, C. E., C. M. Komar, P. A. Cassak, F. D. Wilder, S. Eriksson, and J. F. Drake (2015), Asymmetric  
830 magnetic reconnection with a flow shear and applications to the magnetopause, *J. Geophys. Res. Space*  
831 *Physics*, 120, 7748-7763, doi:10.1002/2015JA021489.  
832 Dougherty, M. K., S. Kellock, D. J. Southwood et al., (2004), The Cassini Magnetic Field  
833 Investigation, *Space Sci. Rev.*, 114, 331-383, doi:10.1007/s11214-004-1432-2.  
834 Dougherty, M. K. et al. (2005), Cassini magnetometer observations during Saturn orbit insertion,  
835 *Science*, 307 (5713), 1266-1270, doi:10.1126/science.1106098.  
836 Dungey, J. W. (1961), Interplanetary magnetic field and the auroral zones, *Physical Review Letters*,  
837 6(2), 47-48, doi: 10.1103/PhysRevLett.6.47.  
838 Fear, R. C., S. E. Milan, J. A. Carter, and R. Maggiolo (2015), The interaction between transpolar arcs  
839 and cusp spots, *Geophys. Res. Lett.*, 42, 9685-9693, doi:10.1002/2015GL066194.  
840 Frey, H. U., S. B. Meade, T. J. Immel, S. A. Fuselier, E. S. Claffin, J.-C. Gérard, and B. Hubert (2002),  
841 Proton aurora in the cusp, *J. Geophys. Res.*, 107(A7), doi:10.1029/2001JA900161.  
842 Fuselier, S. A., H. U. Frey, K. J. Trattner, S. B. Mende, and J. L. Burch (2002), Cusp aurora  
843 dependence on interplanetary magnetic field  $B_z$ , *J. Geophys. Res.*, 107(A7),  
844 doi:10.1029/2001JA900165.  
845 Gérard, J.-C., E. J. Bunce, D. Grodent, S. W. H. Cowley, J. T. Clarke, and S. V. Badman (2005),  
846 Signature of Saturn's auroral cusp: Simultaneous Hubble Space Telescope FUV observations and  
847 upstream solar wind monitoring, *J. Geophys. Res.*, 110, A11201, doi:10.1029/2005JA011094.  
848 Gérard, J.-C., et al. (2006), Saturn's auroral morphology and activity during quiet magnetospheric  
849 conditions, *J. Geophys. Res.*, 111, A12210, doi:10.1029/2006JA011965.  
850 Grodent, D., J.-C. Gérard, S. W. H. Cowley, E. J. Bunce, and J. T. Clarke (2005), Variable morphology  
851 of Saturn's southern ultraviolet aurora, *J. Geophys. Res.*, 110, A07215, doi:10.1029/2004JA010983.  
852 Gustin, J., B. Bonfond, D. Grodent, and J.-C. Gérard (2012), Conversion from HST ACS and STIS  
853 auroral counts into brightness, precipitated power, and radiated power for H2 giant planets, *J. Geophys.*  
854 *Res.*, 117, A07316, doi:10.1029/2012JA017607.  
855 Jackman, C. M., N. Achilleos, E. J. Bunce, S. W. H. Cowley, M. K. Dougherty, G. H. Jones, S. E.  
856 Milan, and E. J. Smith (2004), Interplanetary magnetic field at ~9 AU during the declining phase of the  
857 solar cycle and its implications for Saturn's magnetospheric dynamics, *J. Geophys. Res.*, 109, A11203,  
858 doi:10.1029/2004JA010614.  
859 Jasinski, J. M., et al. (2014), Cusp observation at Saturn's high-latitude magnetosphere by the Cassini  
860 spacecraft, *Geophys. Res. Lett.*, 41, 1382-1388, doi:10.1002/2014GL059319.  
861 Jasinski, J. M. (2015), Cassini Observations of Saturn's Magnetospheric Cusp, doctoral thesis, UCL  
862 (University College London), London, United Kingdom.  
863 Jasinski, J. M., J. A. Slavin, C. S. Arridge, G. Poh, X. Jia, N. Sergis, A. J. Coates, G. H. Jones, and J.  
864 H. Waite Jr. (2016), Flux transfer event observation at Saturn's dayside magnetopause by the Cassini  
865 spacecraft, *Geophys. Res. Lett.*, 43, 6713-6723, doi:10.1002/2016GL069260.  
866 Jinks, S. L., et al. (2014), Cassini multi-instrument assessment of Saturn's polar cap boundary, *J.*  
867 *Geophys. Res. Space Physics*, 119, 8161-8177, doi:10.1002/2014JA020367.  
868 Joy, S. P., M. G. Kivelson, R. J. Walker, K. K. Khurana, C. T. Russell, and W. R. Paterson (2006),  
869 Mirror mode structures in the Jovian magnetosheath, *J. Geophys. Res.*, 111, A12212,  
870 doi:10.1029/2006JA011985.  
871 Kanani, S. J., et al. (2010), A new form of Saturn's magnetopause using a dynamic pressure balance  
872 model, based on in situ, multi-instrument Cassini measurements, *J. Geophys. Res.*, 115, A06207,  
873 doi:10.1029/2009JA014262.  
874 Knight, S. (1973), Parallel electric fields, *Planet. Space Sci.*, 21, 741-751.  
875 Lamy, L., R. Prangé, W. Pryor, J. Gustin, S. V. Badman, H. Melin, T. Stallard, D. G. Mitchell, and P.  
876 C. Brandt (2013), Multispectral simultaneous diagnosis of Saturn's aurorae throughout a planetary  
877 rotation, *J. Geophys. Res. Space Physics*, 118, 4817-4843, doi:10.1002/jgra.50404.

878 Lockwood, M., and J. Moen, 1999, Reconfiguration and closure of lobe flux by reconnection during  
879 northward IMF: possible evidence for signatures in cusp/cleft auroral emissions, *Ann. Geophys.*, 17 (8),  
880 996-1011, doi:10.1007/s005850050827.

881 Masters, A., J. P. Eastwood, M. Swisdak, M. F. Thomsen, C. T. Russell, N. Sergis, F. J. Crary, M. K.  
882 Dougherty, A. J. Coates, and S. M. Krimigis (2012), The importance of plasma  $\beta$  conditions for  
883 magnetic reconnection at Saturn's magnetopause, *Geophys. Res. Lett.*, 39, L08103,  
884 doi:10.1029/2012GL051372.

885 McAndrews, H. J., C. J. Owen, M. Thomsen, B. Lavraud, A. Coates, M. Dougherty, and D. T. Young  
886 (2008), Evidence for reconnection at Saturn's magnetopause, *J. Geophys. Res.*, 113, A04210,  
887 doi:10.1029/2007JA012581.

888 Meredith, C. J., S. W. H. Cowley, K. C. Hansen, J. D. Nichols, and T. K. Yeoman (2013),  
889 Simultaneous conjugate observations of small-scale structures in Saturn's dayside ultraviolet auroras:  
890 Implications for physical origins, *J. Geophys. Res. Space Physics*, 118, 2244-2266,  
891 doi:10.1002/jgra.50270.

892 Meredith, C. J., I. I. Alexeev, S. V. Badman, E. S. Belenkaya, S. W. H. Cowley, M. K. Dougherty, V.  
893 V. Kalegaev, G. R. Lewis, and J. D. Nichols (2014), Saturn's dayside ultraviolet auroras: Evidence for  
894 morphological dependence on the direction of the upstream interplanetary magnetic field, *J. Geophys.  
895 Res. Space Physics*, 119, 1994-2008, doi:10.1002/2013JA019598.

896 Meredith, C. J., Meredith, C. J., S. W. H. Cowley, and J. D. Nichols (2015), Survey of Saturn auroral  
897 storms observed by the Hubble Space Telescope: Implications for storm time scales, *J. Geophys. Res.  
898 Space Physics*, 119, 9624-9642, doi:10.1002/2014JA020601.

899 Milan, S. E., M. Lester, S. W. H. Cowley, and M. Brittner (2000a), Convection and auroral  
900 response to a southward turning of the IMF: Polar UVI, CUTLASS, and IMAGE signatures of transient  
901 magnetic flux transfer at the magnetopause, *J. Geophys. Res.*, 105(A7), 15741-15755,  
902 doi:10.1029/2000JA900022.

903 Milan, S. E., M. Lester, S. W. H. Cowley, and M. Brittner (2000b), Dayside convection and auroral  
904 morphology during an interval of northward interplanetary magnetic field, *Ann. Geophys.*, 18, 436-444,  
905 doi:10.1007/s00585-000-0436-9.

906 Milan, S. E. et al., 2010, Average auroral configuration parameterized by geomagnetic activity and  
907 solar wind conditions, *Ann. Geophys.*, 28 (4), 1003-1012, doi:10.5194/angeo-28-1003-2010.

908 Mitchell, D.G., S.M. Krimigis, C. Paranicas, P.C. Brandt, J.F. Carbary, E.C. Roelof, W.S. Kurth, D.A.  
909 Gurnett, J.T. Clarke, J.D. Nichols, J.-C. Gérard, D. C. Grodent, M. K. Dougherty, and W. R. Pryor  
910 (2009), Recurrent energization of plasma in the midnight-to-dawn quadrant of Saturn's magnetosphere,  
911 and its relationship to auroral UV and radio emissions, *Planetary and Space Science*, 57 (14-15), 1732-  
912 1742, doi:10.1016/j.pss.2009.04.002.

913 Mitchell, D.G., J.F. Carbary, E.J. Bunce, A. Radioti, S.V. Badman, W.R. Pryor, G.B. Hospodarsky, and  
914 W.S. Kurth (2016), Recurrent pulsations in Saturn's high latitude magnetosphere, *Icarus*, 263, 94-100,  
915 http://dx.doi.org/10.1016/j.icarus.2014.10.028.

916 Nichols, J. D., J. T. Clarke, S. W. H. Cowley, J. Duval, A. J. Farmer, J.-C. Gérard, D. Grodent, and S.  
917 Wannawichian (2008), Oscillation of Saturn's southern auroral oval, *J. Geophys. Res.*, 113, A11205,  
918 doi:10.1029/2008JA013444.

919 Nichols, J. D., J. T. Clarke, J. C. Gérard, D. Grodent, and K. C. Hansen (2009), Variation of different  
920 components of Jupiter's auroral emission, *J. Geophys. Res.*, 114, A06210, doi:10.1029/2009JA014051.

921 Nichols, J. D., S. W. H. Cowley, and L. Lamy (2010), Dawn-dusk oscillation of Saturn's conjugate  
922 auroral ovals, *Geophys. Res. Lett.*, 37, L24102, doi:10.1029/2010GL045818.

923 Nichols, J. D., et al. (2014), Dynamic auroral storms on Saturn as observed by the Hubble Space  
924 Telescope, *Geophys. Res. Lett.*, 41, 3323-3330, doi:10.1002/2014GL060186.

925 Nichols, J.D., S.V. Badman, E.J. Bunce, J.T. Clarke, S.W.H. Cowley, G.J. Hunt, and G. Provan (2016),  
926 Saturn's northern auroras as observed using the Hubble Space Telescope, *Icarus*, 263, 17-31,  
927 doi:10.1016/j.icarus.2015.09.008.

928 Øieroset, M., P. E. Sandholt, W. F. Denig, and S. W. H. Cowley (1997), Northward interplanetary  
929 magnetic field cusp aurora and high-latitude magnetopause reconnection, *J. Geophys. Res.*, 102(A6),  
930 11349-11362, doi:10.1029/97JA00559.

931 Palmaerts, B., A. Radioti, E. Roussos, D. Grodent, J.-C. Gérard, N. Krupp, and D. G. Mitchell (2016),  
932 Pulsations of the polar cusp aurora at Saturn, *J. Geophys. Res. Space Physics*, 121, 11,952-11,963,  
933 doi:10.1002/2016JA023497.

934 Pilkington, N. M., N. Achilleos, C. S. Arridge, P. Guio, A. Masters, L. C. Ray, N. Sergis, M. F.  
935 Thomsen, A. J. Coates, and M. K. Dougherty (2015), Internally driven large-scale changes in the size  
936 of Saturn's magnetosphere, *J. Geophys. Res. Space Physics*, 120, 7289-7306,  
937 doi:10.1002/2015JA021290.

938 Provan, G., D. J. Andrews, C. S. Arridge, A. J. Coates, S. W. H. Cowley, S. E. Milan, M. K.  
 939 Dougherty, and D. M. Wright (2009), Polarization and phase of planetary-period magnetic field  
 940 oscillations on high-latitude field lines in Saturn's magnetosphere, *J. Geophys. Res.*, 114, A02225,  
 941 doi:10.1029/2008JA013782.  
 942 Provan, G., S. W. H. Cowley, L. Lamy, E. J. Bunce, G. J. Hunt, P. Zarka, and M. K. Dougherty (2016),  
 943 Planetary period oscillations in Saturn's magnetosphere: Coalescence and reversal of northern and  
 944 southern periods in late northern spring, *J. Geophys. Res. Space Physics*, 121, 9829-9862, Res.  
 945 Space10.1002/2016JA023056.  
 946 Radioti, A., D. Grodent, J.-C. Gérard, S. E. Milan, B. Bonfond, J. Gustin, and W. Pryor (2011),  
 947 Bifurcations of the main auroral ring at Saturn: ionospheric signatures of consecutive reconnection  
 948 events at the magnetopause, *J. Geophys. Res.*, 116, A11209, doi:10.1029/2011JA016661.  
 949 Radioti, A., D. Grodent, J.-C. Gérard, B. Bonfond, J. Gustin, W. Pryor, J. M. Jasinski, and C. S.  
 950 Arridge (2013), Auroral signatures of multiple magnetopause reconnection at Saturn, *Geophys. Res.  
 951 Lett.*, 40, 4498-4502, doi:10.1002/grl.50889.  
 952 Radioti, A., D. Grodent, J.-C. Gérard, S. E. Milan, R. C. Fear, C. M. Jackman, B. Bonfond, and W.  
 953 Pryor (2014), Saturn's elusive nightside polar arc, *Geophys. Res. Lett.*, 41, 6321-6328,  
 954 doi:10.1002/2014GL061081.  
 955 Radioti, A., D. Grodent, X. Jia, J.-C. Gérard, B. Bonfond, W. Pryor, J. Gustin, D. G. Mitchell, and C.  
 956 M. Jackman (2016), A multi-scale magnetotail reconnection event at Saturn and associated flows:  
 957 Cassini/UVIS observations, *Icarus*, 263, 75-82, doi:10.1016/j.icarus.2014.12.016.  
 958 Reiff, P. H. (1982), Sunward convection in both polar caps, *J. Geophys. Res.*, 87 (A8), 5976-5980,  
 959 doi:10.1029/JA087iA08p05976.  
 960 Sanchez-Diaz, E., A. P. Rouillard, B. Lavraud, K. Segura, C. Tao, R. Pinto, N. R. Jr Sheeley, and I.  
 961 Plotnikov (2016), The very slow solar wind: Properties, origin and variability, *J. Geophys. Res. Space  
 962 Physics*, 121, 2830-2841, doi:10.1002/2016JA022433.  
 963 Talboys, D. L., C. S. Arridge, E. J. Bunce, A. J. Coates, S. W. H. Cowley, and M. K. Dougherty  
 964 (2009), Characterization of auroral current systems in Saturn's magnetosphere: High-latitude Cassini  
 965 observations, *J. Geophys. Res.*, 114, A06220, doi:10.1029/2008JA013846.  
 966 Tao, C., R. Kataoka, H. Fukunishi, Y. Takahashi, and T. Yokoyama (2005), Magnetic field variations  
 967 in the Jovian magnetotail induced by solar wind dynamic pressure enhancements, *J. Geophys. Res.*,  
 968 110, A11208, doi:10.1029/2004JA010959.  
 969 Zeiger, B. & K. C. Hansen (2008), Statistical validation of a solar wind propagation model from 1 to 10  
 970 AU, *J. Geophys. Res.*, 113 (8), 1-15, doi:10.1029/2008JA013046.